Hierarchical porous Ni_3S_4 with enriched high-valence Ni sites as a robust electrocatalyst for efficient oxygen evolution reaction

Kai Wan, Jiangshui Luo, Chen Zhou, Ting Zhang, Jordi Arbiol, Xihong Lu*, Bing-Wei Mao, Xuan Zhang*, Jan Fransaer**

K. Wan, Prof. J. Luo, Dr. C. Zhou, Dr. X. Zhang, Prof. J. Fransaer
Department of Materials Engineering
KU Leuven
Leuven 3001, Belgium
E-mail: jiangshui.luo@gmail.com, xuan.zhang@kuleuven.be, jan.fransaer@kuleuven.be

Prof. J. Luo
Collaborative Innovation Center of Clean Energy
Longyan University
Longyan 364012, China
E-mail: jiangshui.luo@gmail.com

T. Zhang, Prof. J. Arbiol
Catalan Institute of Nanoscience and Nanotechnology (ICN2)
CSIC and BIST, Campus UAB
Bellaterra, 08193 Barcelona, Catalonia, Spain

Prof. J. Arbiol
ICREA
Pg. Lluís Companys 23
08010 Barcelona, Spain

Prof. X. H. Lu
MOE of the Key Laboratory of Bioinorganic and Synthetic Chemistry
The Key Lab of Low-carbon Chem and Energy Conservation of Guangdong Province
KLGHEI of Environment and Energy Chemistry
School of Chemistry
Sun Yat-Sen University
Guangzhou 510275, China
E-mail: luxh6@mail.sysu.edu.cn

Prof. J. Luo, Prof. B.-W. Mao
State Key Laboratory of Physical Chemistry of Solid Surfaces and Department of Chemistry
College of Chemistry and Chemical Engineering
Xiamen University
Xiamen 361005, China

Keywords: high-valence Ni^{3+}, hierarchical porous structure, Ni_3S_4, oxygen evolution reaction, durability

Electrochemical water splitting is a common way to produce hydrogen gas, but the sluggish kinetics of oxygen evolution reaction (OER) significantly limits the overall energy conversion efficiency of the water splitting. In this work, a highly active and stable, meso-macro hierarchical porous Ni_3S_4 architecture, enriched in Ni^{3+} was designed as an advanced electrocatalyst for OER. The obtained Ni_3S_4 architectures exhibit a relatively low overpotential of 257 mV at 10 mA cm^{-2}, and 300 mV at 50 mA cm^{-2}. Additionally, this Ni_3S_4 catalyst has excellent long-term stability (no degradation after 300 h at 50 mA cm^{-2}). The outstanding OER performance is due to the high concentration of Ni^{3+} and the meso-macro hierarchical porous structure. The presence of Ni^{3+} enhances the chemisorption of OH^- which facilitates the electron transfer to the surface during OER. The hierarchical porosity increases the number of exposed active sites, and facilitates mass transport. A water-splitting electrolyzer using the prepared Ni_3S_4 as the anode catalyst and Pt/C as the cathode catalyst achieved a low cell voltage of 1.51 V at 10 mA cm^{-2}. Therefore, this work provides a new strategy for the rational design of highly active OER electrocatalysts with high valence Ni^{3+} and hierarchical porous architectures.

1. Introduction

Hydrogen is an environmentally friendly and renewable energy carrier for green energy supply and storage.[1-3] Electrochemical water splitting is one way to produce hydrogen.[4, 5] It involves two half-reactions, the hydrogen evolution reaction (HER) and the oxygen evolution reaction (OER) to produce hydrogen and oxygen, respectively.[6, 7] However, the OER has sluggish kinetics because it is a four-electron transfer process resulting in a high overpotential, which limits the overall energy conversion efficiency of electrochemical water splitting.[8] Currently, IrO_2 and RuO_2 are considered as the best OER catalysts.[9-11] Nevertheless, the scarcity and high cost of Ir and Ru hamper their applications.[7, 12, 13] Hence, it is highly

desirable to develop low cost and earth abundant electrocatalysts with high activity and long-term stability for the OER.

In the past years, substantial efforts have been devoted to exploring transition metal (Fe, Co, Ni) based oxides, and hydroxides as noble-metal-alternative electrocatalysts for OER due to their abundance, low-cost, and high catalytic activity.[14-18] However, their electrochemical application is hindered by some severe obstacles: (1) Low content of high valence state metal ions. The high valence state metal ions such as Co^{3+} and Ni^{3+} have been confirmed as the active sites for OER,[19-23] while most of the work is focused on Co^{2+} and Ni^{2+} based materials.[7, 14, 15] (2) Low utilization efficiency of active sites due to the low specific surface area. (3) Relatively low electrical conductivity of the transition metal-based oxides and hydroxides. In order to solve these issues, various nanostructured nickel sulfide-based materials, such as films of NiS microspheres,[24] Ni_2S_3 nanosheet arrays,[25] Ni_3S_4 nanosheets,[26] porous Ni_9S_8,[27] and hierarchical $NiCo_2S_4$ nanowires,[28] have been developed to achieve high electrocatalytic performance due to their diverse valence states, high specific surface area, and high electrical conductivity. For instance, Qiao *et al.* fabricated a Ni_9S_8/Ni foam electrode for OER which had an overpotential (η) of 340 mV at 30 mA cm^{-2} with a catalyst loading of 11 mg cm^{-2}.[27] Wang *et al.* reported a NiS/Ni foam catalyst with an overpotential of 335 mV at 50 mA cm^{-2} using a catalyst loading of 43 mg cm^{-2}.[24] When Ni_3S_4 (Ni^{2+}, Ni^{3+}) was used as an electrocatalyst, the current density reached 30 mA cm^{-2} at η = 330 mV with a relatively low catalyst loading of 1.2 mg cm^{-2}.[26] Shanmugam *et al.* developed Ni_3S_2/Ni foam and $NiCo_2S_4$/ Ni foam electrodes for OER. The $NiCo_2S_4$/Ni foam (η = 260 mV at 10 mA cm^{-2}, current density loss of 15% after 50 h) showed enhanced electrocatalytic activity and long-term stability compared to Ni_3S_2/Ni (η = 300 mV at 10 mA cm^{-2}, current density loss of 20% after 10 h).[28] Despite the significant progress, the electrocatalytic activities and long-term stability of the most developed nickel sulfides are not yet satisfactory. To this end, the development of alternative electrocatalysts with excellent

electrocatalytic performance and durability for OER is highly challenging and intensively pursued.

In this work, meso-macro hierarchical porous Ni_3S_4 architectures enriched in Ni^{3+} species derived from Ni metal-organic framework (Ni-MOF) is developed as efficient OER electrocatalysts. Metal-organic frameworks (MOFs) with tunable structures and chemical compositions are interesting self-sacrificial templates for the synthesis of nickel sulfides. The as-prepared Ni_3S_4 architectures enriched in Ni^{3+} enhance the chemisorption of OH^- which facilitates the electron transfer. In addition, the obtained meso-macro porous structure increases the number of active sites and facilitates mass transport. Due to the enhanced chemisorption of OH^-, the high number of active sites, and the easy mass transport, the Ni_3S_4 architectures exhibit a remarkable OER performance. The Ni_3S_4 catalyst on Ni foam (NM50-Ni_3S_4/NF) electrode shows a relatively low overpotential of 257 mV at 10 mA cm^{-2}, and 300 mV at 50 mA cm^{-2}. The NM50-Ni_3S_4/NF electrode exhibits not only outstanding electrocatalytic activity but also excellent long-term stability even at a high current density (no degradation after 300 h at 50 mA cm^{-2}). Furthermore, a water-splitting electrolyzer using NM50-Ni_3S_4/NF as the anode catalyst and Pt/C as the cathode catalyst achieves a low cell voltage of 1.51 V at 10 mA cm^{-2}.

2. Results and discussion

The Ni_3S_4 catalysts were synthesized as illustrated in **Figure 1**a. Firstly, the Ni-MOFs were prepared by dissolving Ni salt and organic linkers in DMF by a solvothermal method.[29, 30] Scanning electron microscopy (SEM) images reveal that the Ni-MOFs consist of large round plates with an average diameter of around 100 μm and an average thickness of around 6 μm (Figure 1b-c and Figure S1, Supporting Information). Disk-like particles with a larger thickness could be obtained by increasing the growth temperature (Figure S1). [31, 32] X-ray diffraction (XRD) patterns of the obtained MOFs exhibit the same diffraction peaks as the theoretical pattern (Figure 1d),[29] indicating the successful synthesis of Ni-MOFs. Next, the

Ni-MOFs underwent a solvothermal process to obtain Ni_3S_4. The as-synthesized NM50-Ni_3S_4 shows a large nanoflake structure resembling the Ni-MOF template (Figure 1e). Electron energy loss spectroscopy (EELS) spectra (Figure 1f) confirm that nickel sulfide was obtained by this solvothermal method with a uniform distribution of Ni and S. High resolution transmission electron microscopy (HRTEM) images (Figure 1g) indicate that the nickel sulfide has good crystallinity. The lattice fringe distances were measured to be 0.536 nm, 0.493 nm, 0.551 and 0.242 nm, respectively, which are reminiscent of the cubic Ni_3S_4 phase (Table S1, Supporting Information). The magnified detail of the area highlighted in yellow and its corresponding power spectrum reveal that the structure of the selected region is in agreement with the cubic phase of Ni_3S_4 (space group: Fd3mS) with $a = b = c = 0.94570$ nm.

XRD was employed to characterize the obtained nickel sulfide (**Figure 2**a, Figure S2, Supporting Information). The typical diffraction pattern of polydymite was observed. The diffraction peaks at 2θ of 26.6°, 31.2°, 37.9°, 47.0°, 49.9°, and 54.7° correspond to the (220), (311), (400), (422), (511), and (440) planes of cubic Ni_3S_4 (JCPDS: 00-047-1739), respectively.[33] The Ni_3S_4 sample derived from NM120 precursor shows an additional peak at *ca.* 30°, which may be due to the incomplete sulfurization caused by its larger thickness (*ca.* 75 μm). Raman spectra (Figure 2b) reveal that the vibrational bands at 224 cm^{-1}, 286 cm^{-1}, 337 cm^{-1} and 379 cm^{-1} in the low wavenumber region are attributed to Ni_3S_4,[34, 35] confirming that these samples are Ni_3S_4. Nitrogen ad/desorption isotherm and pore size distribution plots were used to investigate the porous structure of Ni_3S_4 catalysts (Figure 2c-d). The typical type-IV isotherms at a relative pressure of *ca.* 0.5-1.0 with an H3 hysteresis loop indicate a hierarchical porous structure and a broad pore-size distribution.[36-38] The specific surface areas of the obtained nickel sulfides are 34, 23 and 14 $m^2\ g^{-1}$ for NM50-Ni_3S_4, NM80-Ni_3S_4 and NM120-Ni_3S_4, respectively.

X-ray photoelectron spectroscopy (XPS) was employed to investigate the elemental composition and chemical state of the surface of these Ni_3S_4 samples (**Figure 3**, Figure S4,

and Table S2-S4, Supporting Information). XPS detected C, N, O, S, and Ni. The C, N, and O come from the residue of the Ni-MOFs linkers. The rather high oxygen content in the samples might originate from the surface oxidation of Ni_3S_4.[39] The Ni 2p spectrum of NM50-Ni_3S_4 was deconvoluted into eight peaks, which were assigned to the Ni $2p_{3/2}$, Ni $2p_{1/2}$, and satellite peaks (Figure 3b). For the Ni $2p_{3/2}$, the binding energies at 852.99, 852.93, 852.64, 852.64 and 852.80 eV and 856.57, 586.50, 855.59, 855.88 and 856.03 eV were assigned to Ni^{2+} and Ni^{3+}, respectively.[40, 41] The peaks at 860.35 ± 0.2 eV and 863.35 ± 0.2 eV were assigned to the satellite peaks (referred as 'Sat.' in the figure), which indicate the presence of nickel–oxygen species.[42-44] The peak area of the Ni^{3+} 2p was much larger than that of Ni^{2+} 2p, demonstrating the much higher content of Ni^{3+}. Figure 3c summarizes the content of Ni^{2+} and Ni^{3+} in these samples, of which the Ni^{3+} content is ten times higher than that of Ni^{2+}. The NM50-Ni_3S_4 exhibits the highest Ni content, as well as the highest Ni^{3+} content. Ni^{3+} improves the electrophilicity of adsorbed oxygen and therefore benefits the formation of NiOOH through nucleophilic attack during OER and is generally regarded as the active site for OER.[21, 23] For the S 2p spectrum, the peaks at 161.3 eV, 162.6 eV, and 164.3 eV were attributed to the S $2p_{3/2}$ of S^{2-}, S $2p_{1/2}$ of S^{2-}, and the bridging S_2^{2-} (referred to as 'SO_4^{2-}'), respectively (Figure 3d)[39, 45, 46].

The electrocatalytic activity of the Ni_3S_4 catalysts for OER was investigated in 1.0 M KOH on a glassy carbon electrode (**Figure 4**, Figure S5, Supporting Information). The peaks at 1.38 V and 1.28 V *vs.* RHE refer to the redox reaction of Ni^{2+} to Ni^{3+} that goes forward and backward, respectively.[47-49] When scanning to more positive potentials than 1.5 V *vs.* RHE, the current density rapidly increases due to oxygen evolution. The overpotential (η) at a current density of 10 mA cm^{-2} was employed to evaluate the electrocatalytic activity of OER.[50] It is seen that all tested Ni_3S_4 catalysts show a lower overpotential than IrO_2 at a current density of 10 mA cm^{-2} (Figure 4b). The NM50-Ni_3S_4 shows an overpotential of 0.307 V at a current density of 10 mA cm^{-2} with a Tafel slope of 67 mV dec^{-1} (Figure 4c). A Tafel slope between 40 and 120

mV dec^{-1} indicates that the OER on NM50-Ni_3S_4 may be controlled by the chemisorption of OH^- and the formation of *-O^- of the Krasil'shcikov path (Supporting Information).[51-53] The charge transfer resistance (R_{ct}) of the Ni_3S_4 catalysts for the OER was evaluated by electrochemical impedance spectroscopy (Figure S6, Supporting Information) at an applied potential of 1.61 V *vs.* RHE. It can be seen that the NM50-Ni_3S_4 sample shows the smallest charge transfer resistance (19 Ω), resulting in the highest current density at high overpotential. The Faradaic efficiency of NM50-Ni_3S_4 for the OER was found to be around 99%, indicating that nearly all of the current was used for the evolution of oxygen (Figure S7, Supporting Information).

The NM50-Ni_3S_4 catalyst was coated on a Ni foam electrode (NM50-Ni_3S_4/NF) and tested for OER (Figure 4d, Figure S8 and Figure S9 in Supporting Information). The contribution of the Ni foam to the OER can be ignored (Figure 4d). The NM50-Ni_3S_4/NF electrode shows much higher OER performance than IrO_2 and Ni foam. The NM50-Ni_3S_4/NF electrode reached a current density of 10 mA cm^{-2}, 50 mA cm^{-2}, and 100 mA cm^{-2} at an overpotential of 0.257 V, 0.300 V, and 0.340 V, respectively, making it one of the best nickel sulfide OER catalysts reported in literature (Table S5, Supporting Information). The NM50-Ni_3S_4/NF electrode shows excellent long-term stability at 50 mA cm^{-2}, while the overpotential of IrO_2 for OER rapidly increased by 73 mV after 4000 s (Figure 4e). Finally, a full water-splitting electrolyzer was fabricated by using NM50-Ni_3S_4/NF as the anode catalyst and Pt/C as the cathode catalyst. A relatively low cell voltage of 1.51 V was achieved at 10 mA cm^{-2}, and almost no degradation after operation at 20 mA cm^{-2} for 30 h (Figure 4f).

To gain further insights into the electrocatalytic OER activity of the Ni_3S_4, density functional theory (DFT) was employed to calculate the chemisorption free energies of OH^- on the surface of Ni_3S_4 (**Figure 5**). There are two kinds of coordinated Ni ions in the crystal structure of Ni_3S_4, *viz.* the tetracoordinated Ni_4 (a Ni atom coordinated with four S atoms, Ni^{2+}) and hexacoordinated Ni_6 (a Ni atom coordinated with six S atoms, Ni^{3+}) (Figure 5a-b).

The (110) plane of Ni_3S_4 was selected to calculate the chemisorption free energies of OH^-, due to the fact that this plane contains both kinds of Ni sites simultaneously. The hexacoordinated Ni_6 exhibits an OH^- chemisorption free energy of 0.16 eV, which is much lower than 1.01 eV for that of the tetracoordinated Ni_4, revealing the strong chemisorption capacity of hexacoordinated Ni_6 (Figure 5b). The electron will be transfered from the adsorbed OH^- to the surface Ni sites during the OER process. The calculations show that the OH^- adsorbed on the hexacoordinated Ni_6 exhibits a more positive charge density (red area around OH^-) than that of tetracoordinated Ni_4, facilitating the electron transfer to the Ni surface sites. The O-H band adsorbed on the hexacoordinated Ni_6 shows an enhanced activation thus yielding a shorter Ni-O band distance (1.827 Å) and a longer O-H band (0.983 Å) (Figure 5c-d).

Therefore, the outstanding OER performance of the Ni_3S_4 electrocatalyst is attributed to the following. Firstly, the Ni^{3+} is beneficial for the chemisorption of OH^- on the surface of Ni_3S_4 which facilitates the electron transfer from the OH^- to the surface Ni sites during OER. Secondly, the hierarchical porous structure provides more active sites per projected surface area and meanwhile enables faster mass transfer.

3. Conclusions

A hierarchical porous Ni^{3+}-rich Ni_3S_4 material was synthesized and tested as an OER electrocatalyst. The Ni_3S_4 architecture exhibits high electrocatalytic activity for OER (with an overpotential of 257 mV at 10 mA cm^{-2} and 300 mV at 50 mA cm^{-2}) and excellent long-term stability (no degradation after 300 h at 50 mA cm^{-2}). The outstanding OER performance is attributed to the high concentration of Ni^{3+} on the surface which favors the adsorption of OH^-, and the increased number of active sites and the fast mass transport originating from the hierarchical porous architectures. This work thus provides a strategy for the design of highly active OER electrocatalysts with enriched Ni^{3+} sites and hierarchical porous architectures, which can be extended to other transition metal sulfides for various applications not limited to

OER.

4. Experimental section

4.1. Materials preparation

Preparation of Ni-MOF: The Ni(HBTC)(4,4′-bipy)·3DMF metal-organic framework was synthesized by a mild solvothermal method modified from previous work.[29, 30] Typically, 8.73 g $Ni(NO_3)_2 \cdot 6H_2O$ (99% purity, Acros Organics), 2.11 g trimesic acid (H_3BTC, 98% purity, ABCR Germany), and 1.92 g 4,4-dipyridyl (98 % purity, Acros Organics) were dissolved in 200 mL N,N-dimethylformamide (DMF, ≥ 99%, Chem-Lab). This mixture was heated at 50 °C, 80 °C, and 120 °C for 72 h, respectively. The final light green products were washed with DMF and ethanol (EtOH, 99.9% purity, VWR France) and dried in air at 60 °C overnight. The Ni-MOFs synthesized at 50 °C, 80 °C, and 120 °C were denoted as NM50, NM80 and NM120, respectively.

Preparation of Ni_3S_4 catalysts: The Ni-MOFs were converted into Ni_3S_4 through a solvothermal method in EtOH at 150 °C for 12 h using sodium sulfide ($Na_2S \cdot 9H_2O$, >98%, Acros Organics) as a sulfur source. The molar ratio of the Ni-MOFs to $Na_2S \cdot 9H_2O$ was 1 : 8. After reaction, the obtained suspension was centrifuged and the solids were washed with EtOH and deionized water, and dried in air at 60 °C overnight. The resulting black powders were denoted as NM50-Ni_3S_4, NM80-Ni_3S_4 and NM120-Ni_3S_4, respectively.

4.2. Physicochemical characterizations

X-ray diffraction (XRD) patterns were recorded on a Bruker AXS D8 diffractometer using Cu Kα radiation (λ = 0.15405 nm) and Ni filter with 2θ ranging from 5° to 80° with a step size of 0.02° (1.0 s per step) at 40 kV. Raman spectra were obtained from a LabRAM Aramis spectrometer with a 632.81 nm helium-neon laser. X-ray photoelectron spectroscopy (XPS) was performed with a PHI quantum-2000 (monochromatic Al Kα with 1486.6 eV operating at 15 kV and 300 W). The morphologies and microstructures were observed on a FEI Nova NanoSEM 450 scanning electron microscopy (SEM). High resolution transmission electron

microscopy (HRTEM) and scanning transmission electron microscopy (STEM) images were obtained on a FEI Tecnai F20 field emission gun microscope operated at 200 kV with a point-to-point resolution of 0.19 nm, which is equipped with high angle annular dark field (HAADF) and an electron energy loss spectroscopy (EELS) GATAN Quantum detectors. The energy dispersive spectroscopy (EDS) was measured at 15.0 kV. In order to improve the surface electronic conductivity of the MOFs, the MOF-covered metal plate was sputtered with a 10 nm layer of Pt. The pore structures of samples were probed by nitrogen adsorption/desorption isotherms at 77 K (Micromeritics ASAP 2020, US). Prior to the measurements, the samples were outgassed at 100 °C for 12 h. The specific surface area was determined by the Brunauer-Emmett-Teller (BET) model, while the pore size and volume were calculated by the density functional theory (DFT) method of the built-in software.

4.3. Electrochemical measurements

All the electrochemical properties were characterized using an Autolab electrochemical workstation at room temperature (25 °C). A three-electrode system with a graphite plate (1 cm × 5 cm) as the counter electrode and a Hg/HgO electrode (Tianjin Aida Hengsheng Technology Co. Ltd., China) as the reference electrode was used. The obtained Ni_3S_4 catalysts coated on a glassy carbon disk (5.0 mm in diameter, PINE) or Ni foam (Suzhou Taili Material Technology Co., Ltd., China) was employed as the working electrode. The OER polarization curve of IrO_2 (P40V020, particles from Premetek Co.) was recorded for comparison. To evaluate the electrocatalytic activity of the OER, the cyclic voltammograms were recorded at 10 mV s^{-1} in the potential range between 0.98 and 1.73 V *vs.* RHE on a rotating disk electrode at a rotating speed of 1600 rpm in oxygen-saturated 1.0 M KOH solution. The long-term stability was carried out with a NM50-Ni_3S_4/NF electrode (NM50-Ni_3S_4 coated on Ni foam) by chronoamperometry at 50 mA cm^{-2} in 1.0 M KOH solution. The NM50-Ni_3S_4/NF electrode was also used as the anode in a water-splitting electrolyzer using Pt/C on Ni foam as the cathode, operating at 20 mA cm^{-2}. The EIS measurements were recorded in a frequency

range from 100 kHz to 0.1 Hz with an amplitude of 5 mV (peak-to-peak) at an applied potential of 1.61 V *vs.* RHE.

Supporting Information

Supporting Information is available from the Wiley Online Library or from the author.

Acknowledgements

K. Wan is grateful to the Oversea Study Program of Guangzhou Elite Project. The Open Project Program of Provincial Key Laboratory of Clean Energy Materials, Longyan University (QJNY-201705) is also acknowledged. X. Zhang is grateful to the China Scholarship Council. J. Luo acknowledges the Research Foundation – Flanders (FWO) for a Research Project (G0B3218N) and a Research Grant (1529816N). Funding from the National Natural Science Foundation of China (No. 21776120), and "Minjiang Scholar" Program and key project (No. JZ160480) of Department of Education, Fujian Province, China is also acknowledged. ICN2 members acknowledge funding from Generalitat de Catalunya 2017 SGR 327 and the Spanish MINECO project VALPEC (ENE2017-85087-C3). ICN2 acknowledges support from the Severo Ochoa Programme (MINECO, Grant no. SEV-2013-0295) and is funded by the CERCA Programme / Generalitat de Catalunya. Part of the present work has been performed in the framework of Universitat Autònoma de Barcelona Materials Science PhD program. T. Zhang has received funding from the CSC-UAB PhD scholarship program.

Received: ((will be filled in by the editorial staff))
Revised: ((will be filled in by the editorial staff))
Published online: ((will be filled in by the editorial staff))

References

[1] Y. Bo, S. Yujie, *Accounts Chem. Res.* **2018**.

[2] J. Wang, F. Xu, H. Jin, Y. Chen, Y. Wang, *Adv. Mater.* **2017**, 29, 1605838.

[3] J. Wang, W. Cui, Q. Liu, Z. Xing, A. M. Asiri, X. Sun, *Adv. Mater.* **2016**, 28, 215.

[4] K. C. Nitin, J. Haneul, K. Byeongyoon, L. Kwangyeol, *Nanoscale* **2017**.

[5] X. Zou, Y. Zhang, *Chem. Soc. Rev.* **2015**, 44, 5148.

[6] J. Zhou, Y. Dou, A. Zhou, R. M. Guo, M. J. Zhao, J. R. Li, *Adv. Energy Mater.* **2017**, 7, 1602643.

[7] J. S. Kim, B. Kim, H. Kim, K. Kang, *Adv. Energy Mater.* **2018**, 8, 1702774.

[8] L. Zhuang, L. Ge, Y. Yang, M. Li, Y. Jia, X. Yao, Z. Zhu, *Adv. Mater.* **2017**, 29, 1606793.

[9] S. Cherevko, S. Geiger, O. Kasian, N. Kulyk, J.-P. Grote, A. Savan, B. R. Shrestha, S. Merzlikin, B. Breitbach, A. Ludwig, K. J. J. Mayrhofer, *Catal. Today* **2016**, 262, 170.

[10] E. A. Paoli, F. Masini, R. Frydendal, D. Deiana, C. Schlaup, M. Malizia, T. W. Hansen, S. Horch, I. E. L. Stephens, I. Chorkendorff, *Chem. Sci.* **2015**, 6, 190.

[11] D. Y. Kuo, J. K. Kawasaki, J. N. Nelson, J. Kloppenburg, G. Hautier, K. M. Shen, D. G. Schlom, J. Suntivich, *J. Am. Chem. Soc.* **2017**, 139, 3473.

[12] N. T. Suen, S. F. Hung, Q. Quan, N. Zhang, Y. J. Xu, H. M. Chen, *Chem. Soc. Rev.* **2017**, 46, 337.

[13] D. Chen, C. Chen, Z. M. Baiyee, Z. Shao, F. Ciucci, *Chem. Rev.* **2015**, 115, 9869.

[14] Y. Jingfang, W. Qiang, O. H. Dermot, S. Luyi, *Chem. Soc. Rev.* **2017**.

[15] M. S. Burke, L. J. Enman, A. S. Batchellor, S. Zou, S. W. Boettcher, *Chem. Mater.* **2015**, 27, 7549.

[16] F. Dionigi, P. Strasser, *Adv. Energy Mater.* **2016**, 6, 1600621.

[17] X. Zhang, J. Luo, K. Wan, D. Plessers, B. Sels, J. Song, L. Chen, T. Zhang, P. Tang, J. R. Morante, J. Arbiol, J. Fransaer, *J. Mater. Chem. A* **2019**, 7, 1616.

[18] X. Zhang, J. Luo, H. F. Lin, P. Tang, J. R. Morante, J. Arbiol, K. Wan, B. W. Mao, L. M. Liu, J. Fransaer, *Energy Storage Mater.* **2019**, 17, 46.

[19] B. Zhang, X. Zheng, O. Voznyy, R. Comin, M. Bajdich, M. Garcia-Melchor, L. Han, J. Xu, M. Liu, L. Zheng, F. P. Garcia de Arquer, C. T. Dinh, F. Fan, M. Yuan, E. Yassitepe, N. Chen, T. Regier, P. Liu, Y. Li, P. De Luna, A. Janmohamed, H. L. Xin, H. Yang, A. Vojvodic, E. H. Sargent, *Science* **2016**, 352, 333.

[20] M. Görlin, P. Chernev, J. Ferreira de Araújo, T. Reier, S. Dresp, B. Paul, R. Krähnert, H. Dau, P. Strasser, *J. Am. Chem. Soc.* **2016**, 138, 5603.

[21] H. Y. Wang, Y. Y. Hsu, R. Chen, T. S. Chan, H. M. Chen, B. Liu, *Adv. Energy Mater.* **2015**, 5, 1500091.

[22] D. Friebel, M. W. Louie, M. Bajdich, K. E. Sanwald, Y. Cai, A. M. Wise, M. J. Cheng, D. Sokaras, T. C. Weng, R. Alonso-Mori, R. C. Davis, J. R. Bargar, J. K. Norskov, A. Nilsson, A. T. Bell, *J. Am. Chem. Soc.* **2015**, 137, 1305.

[23] M. Tahir, L. Pan, R. Zhang, Y. C. Wang, G. Shen, I. Aslam, M. A. Qadeer, N. Mahmood, W. Xu, L. Wang, X. Zhang, J. J. Zou, *ACS Energy Lett.* **2017**, 2, 2177.

[24] W. Zhu, X. Yue, W. Zhang, S. Yu, Y. Zhang, J. Wang, J. Wang, *Chem. Commun.* **2016**, 52, 1486.

[25] L. L. Feng, G. Yu, Y. Wu, G. D. Li, H. Li, Y. Sun, T. Asefa, W. Chen, X. Zou, *J. Am. Chem. Soc.* **2015**, 137, 14023.

[26] J. T. Ren, Z. Y. Yuan, *ACS Sustain. Chem. Eng.* **2017**, 5, 7203.

[27] G. F. Chen, T. Y. Ma, Z. Q. Liu, N. Li, Y. Z. Su, K. Davey, S. Z. Qiao, *Adv. Funct. Mater.* **2016**, 26, 3314.

[28] A. Sivanantham, P. Ganesan, S. Shanmugam, *Adv. Funct. Mater.* **2016**, 26, 4661.

[29] Y. Li, L. Xie, Y. Liu, R. Yang, X. Li, *Inorg. Chem.* **2008**, 47, 10372.

[30] K. Jayaramulu, J. Masa, O. Tomanec, D. Peeters, V. Ranc, A. Schneemann, R. Zboril, W. Schuhmann, R. A. Fischer, *Adv. Funct. Mater.* **2017**, 27, 1700451.

[31] E. Biemmi, S. Christian, N. Stock, T. Bein, *Microporous Mesoporous Mater.* **2009**, 117, 111.

[32] N. Stock, S. Biswas, *Chem. Rev.* **2012**, 112, 933.

[33] W. Pan, Y. Huang, S. Cui, W. Chen, L. Mi, *ChemistrySelect* **2016**, 1, 3618.

[34] Z. Cheng, M. Liu, *Solid State Ionics* **2007**, 178, 925.

[35] J. Deng, Q. Gong, H. Ye, K. Feng, J. Zhou, C. Zha, J. Wu, J. Chen, J. Zhong, Y. Li, *ACS Nano* **2018**, 12, 1829.

[36] M. Thommes, K. Kaneko, A. V. Neimark, J. P. Olivier, F. Rodriguez-Reinoso, J. Rouquerol, K. S. W. Sing, *Pure Appl. Chem.* **2015**, 87.

[37] K. Wan, A. D. Tan, Z. P. Yu, Z. X. Liang, J. H. Piao, P. Tsiakaras, *Appl. Catal. B Environ.* **2017**, 209, 447.

[38] K. Wan, Z. P. Yu, Q. B. Liu, J. H. Piao, Y. Y. Zheng, Z. X. Liang, *RSC Adv.* **2016**, 6, 75058.

[39] J. Lv, Y. Cheng, W. Liu, B. Quan, X. Liang, G. Ji, Y. Du, *J. Mater. Chem. C* **2018**, 6, 1822.

[40] X. Ma, L. Zhang, G. Xu, C. Zhang, H. Song, Y. He, C. Zhang, D. Jia, *Chem. Eng. J.* **2017**, 320, 22.

[41] B. Guan, Y. Li, B. Yin, K. Liu, D. Wang, H. Zhang, C. Cheng, *Chem. Eng. J.* **2017**, 308, 1165.

[42] K. Lian, S. Thorpe, D. Kirk, *Electrochim. Acta* **1992**, 37, 2029.

[43] P. Selvam, B. Viswanathan, V. Srinivasan, *J. Electron Spectrosc. Relat. Phenom.* **1989**, 49, 203.

[44] B. Konkena, J. Masa, A. J. R. Botz, I. Sinev, W. Xia, J. Koßmann, R. Drautz, M. Muhler, W. Schuhmann, *ACS Catal.* **2017**, 7, 229.

[45] F. Huang, Y. W. Sui, F. X. Wei, J. Q. Qi, Q. K. Meng, Y. Z. He, *J. Mater. Sci.: Mater. Electron.* **2018**, 29, 2525.

[46] Z. Zhang, Q. Wang, C. Zhao, S. Min, X. Qian, *ACS Appl. Mater. Interfaces* **2015**, 7, 4861.

[47] T. Pitchai, M. Viruthasalam, S. Velu, S. Marappan, *Catal. Sci. Technol.* **2017**.

[48] J. S. Chen, J. Ren, M. Shalom, T. Fellinger, M. Antonietti, *ACS Appl. Mater. Interfaces* **2016**, 8, 5509.

[49] L. K. Wu, W. Y. Wu, J. Xia, H. Z. Cao, G. Y. Hou, Y. P. Tang, G. Q. Zheng, *J. Mater. Chem. A* **2017**, 5, 10669.

[50] J. Luo, J.-H. Im, M. T. Mayer, M. Schreier, M. K. Nazeeruddin, N.-G. Park, S. D. Tilley, H. J. Fan, M. Grätzel, *Science* **2014**, 345, 1593.

[51] E. L. Miller, R. E. Rocheleau, *J. Electrochem. Soc.* **1997**, 144, 3072.

[52] H. Xiao, H. Shin, W. A. Goddard, *Proc. Natl. Acad. Sci. U. S. A.* **2018**, 115, 5872.

[53] S. Gupta, L. Qiao, S. Zhao, H. Xu, Y. Lin, S. V. Devaguptapu, X. Wang, M. T. Swihart, G. Wu, *Adv. Energy Mater.* **2016**, 6, 1601198.

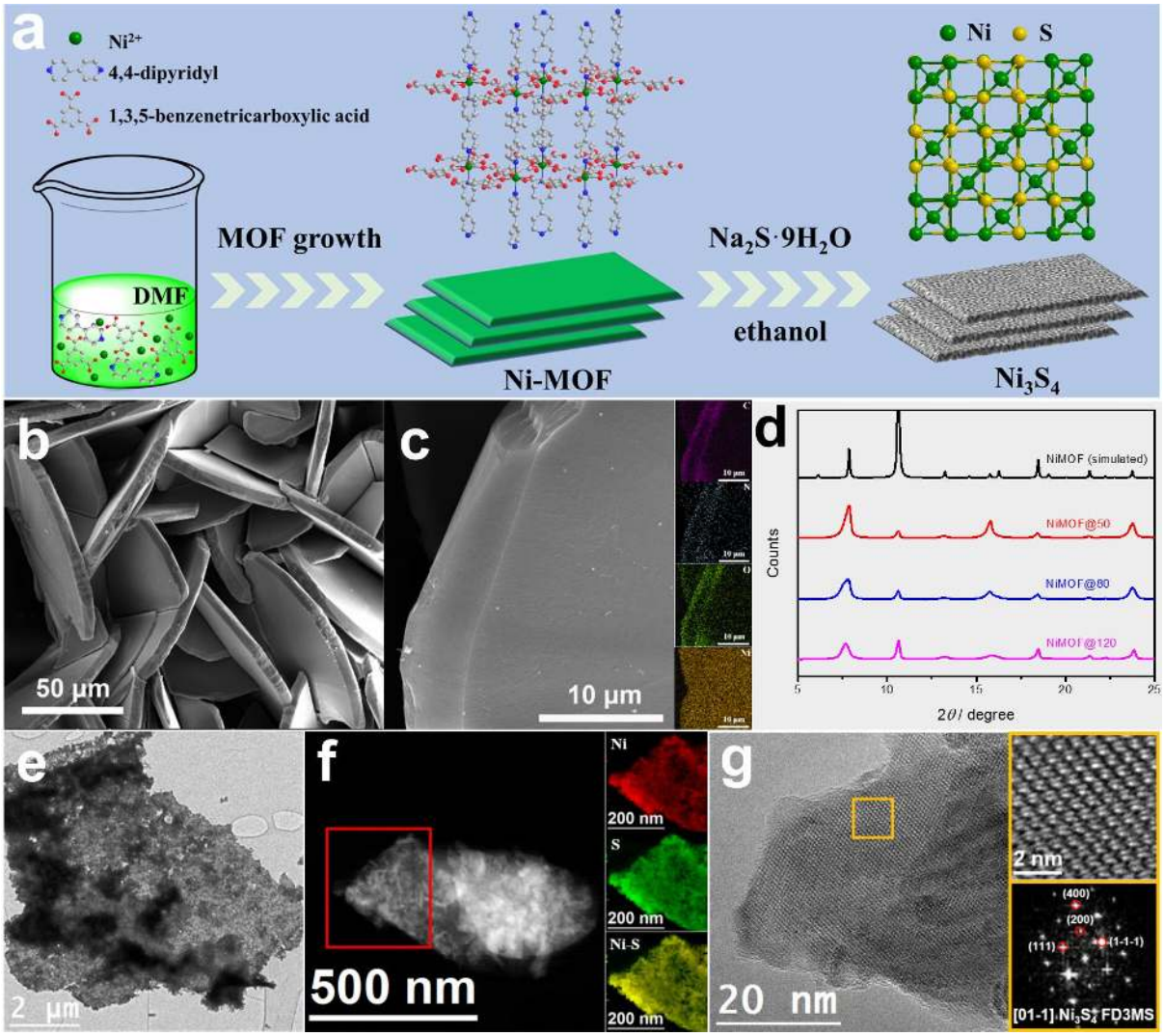

Figure 1. a) schematic illustration of the synthesis method. b) SEM images of NM50. c) EDS elemental mapping images of the NM50. d) X-ray diffraction (XRD) patterns of the obtained Ni-MOFs. e) TEM images of NM50-Ni_3S_4. f) EELS chemical composition maps of NM50-Ni_3S_4 obtained from the area highlighted in red in the STEM micrograph. g) HRTEM micrograph of NM50-Ni_3S_4 (with the selected area highlighted in yellow) and its corresponding power spectrum.

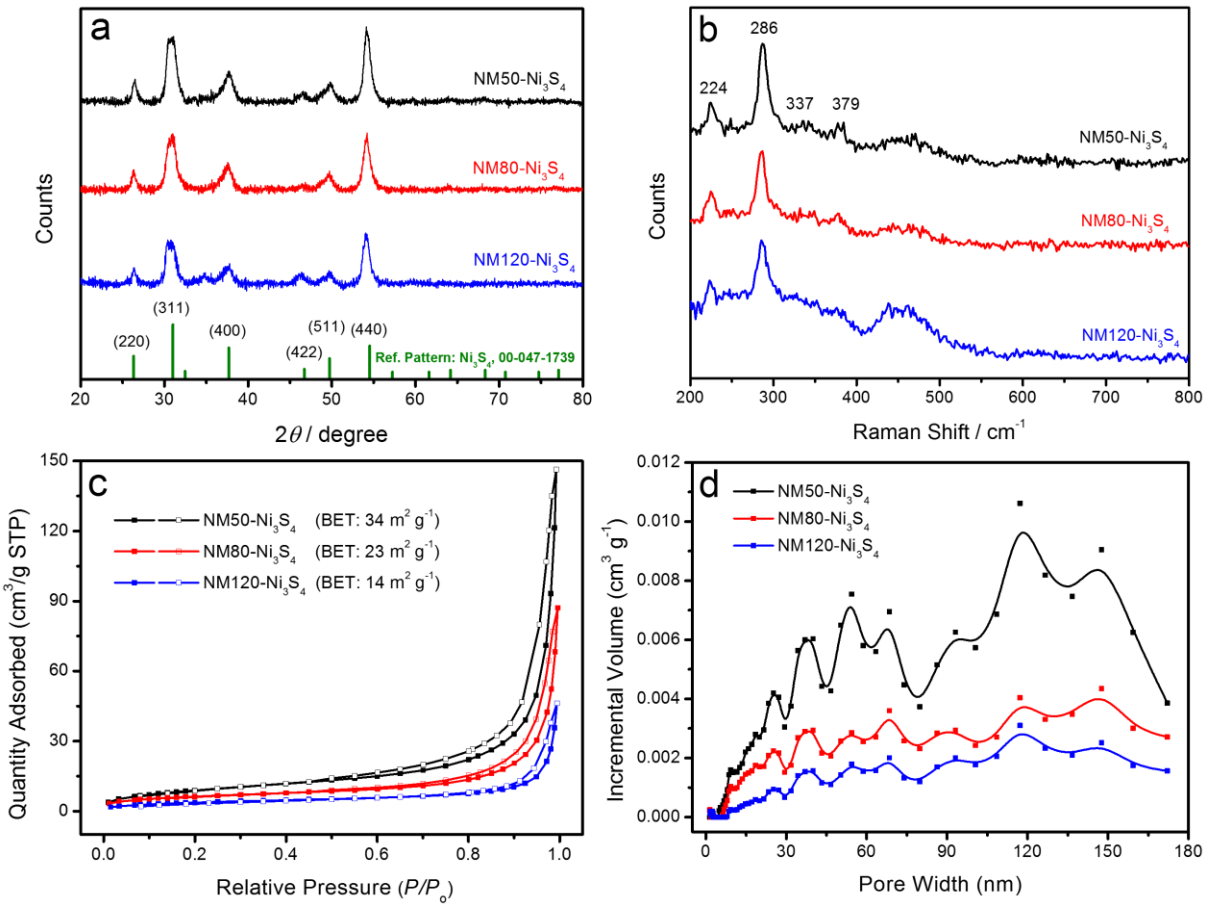

Figure 2. a) X-ray diffraction (XRD) patterns of the Ni_3S_4 catalysts. b) Raman spectra of the Ni_3S_4 catalysts. c) Nitrogen ad/desorption isotherms of the Ni_3S_4 catalysts and d) the corresponding pore size distribution.

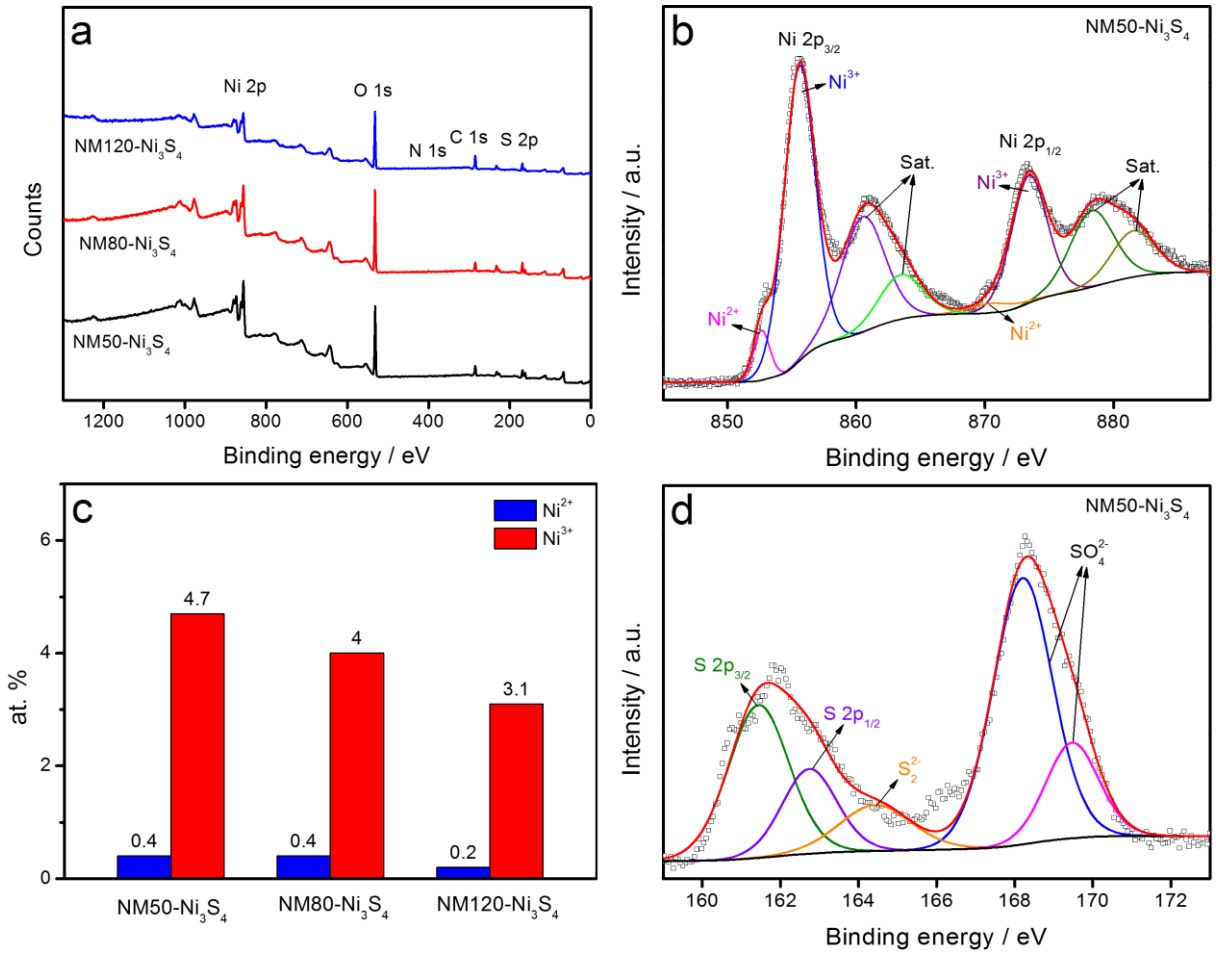

Figure 3. a) XPS survey spectra of the Ni_3S_4 catalysts. b) Ni 2p peaks and the peak fitting results of the NM50-Ni_3S_4 catalyst. c) Ni^{2+} and Ni^{3+} content extracted from XPS results. d) S 2p peak and the peak fitting results of the NM50- Ni_3S_4 catalyst.

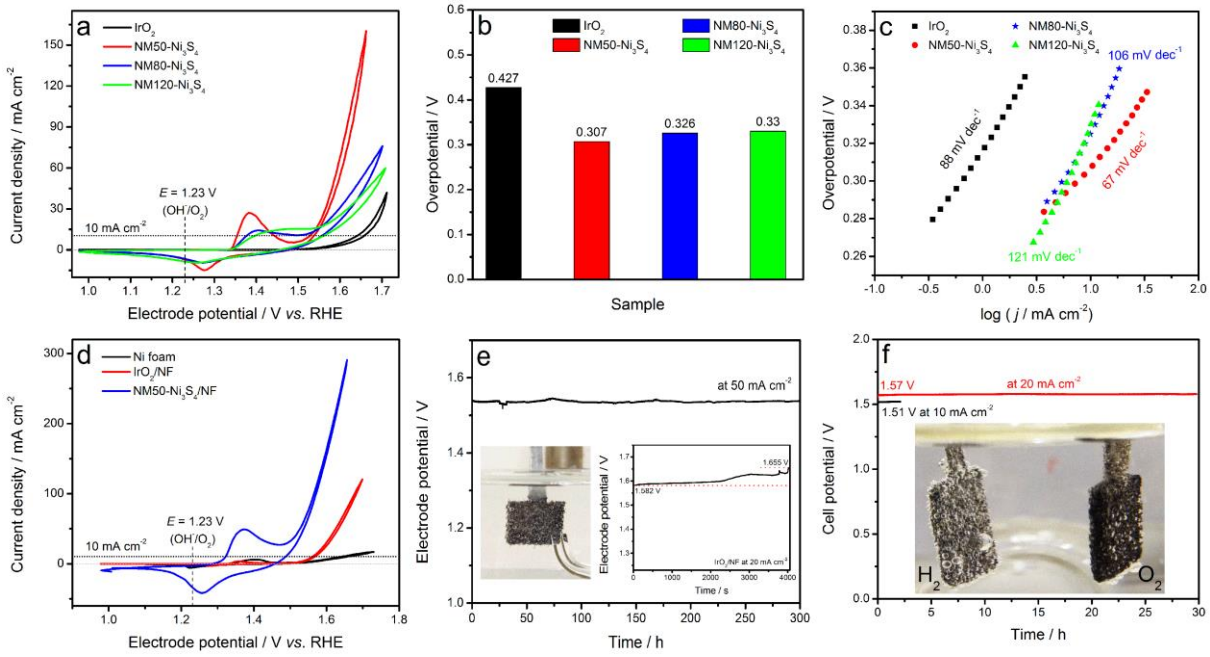

Figure 4. a) Cyclic voltammograms of the Ni_3S_4 in 1.0 M KOH at a scan rate of 10 mV s^{-1} at 1600 rpm. b) The corresponding overpotentials at a current density of 10 mA cm^{-2} extracted from the backward scan from 1.73 V to 0.98 V *vs.* RHE. c) The corresponding Tafel plots of the Ni_3S_4 catalysts. d) Cyclic voltammograms of Ni_3S_4 on Ni foam in 1.0 M KOH at a scan rate of 10 mV/s. e) Long-term stability test at 50 mA cm^{-2} in 1.0 M KOH (inset: photograph of the anode during O_2 evolution and chronopotentiometric curves of IrO_2 on Ni foam). f) Full water splitting at 20 mA cm^{-2} in 1.0 M KOH (anode: NM50-Ni_3S_4/NF, cathode: 10 wt. % Pt/C; insert: a photograph of anode and cathode during water splitting).

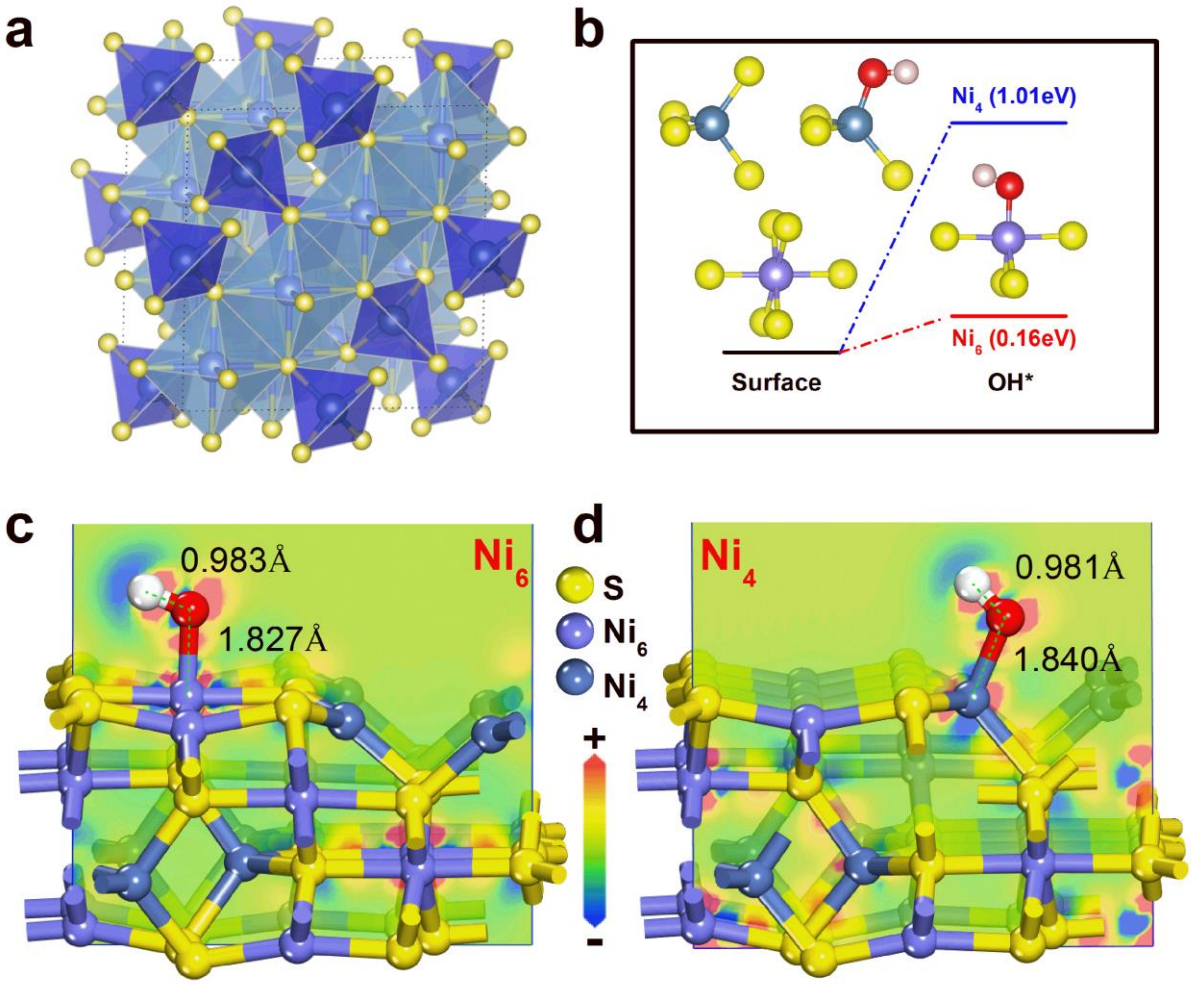

Figure 5. a) The crystal structure of Ni_3S_4. b) Chemisorption free energies of OH^- on the (110) plane of Ni_3S_4; Insert: low-valence (Ni^{2+}) tetracoordinated Ni_4 and high-valence (Ni^{3+}) hexacoordinated Ni_6. c) The electron density difference of OH^- adsorbed on Ni^{3+}. d) The electron density difference of OH^- adsorbed on Ni^{2+}.

The Ni_3S_4 enriched with high-valence Ni^{3+} enhance the chemisorption of OH^-, which facilitates the electron transfer from the OH^- to the surface Ni sites during OER. The hierarchical porous structure enables high number of active sites, and faster mass transfer.

High-valence Ni^{3+}

K. Wan, J. Luo*, C. Zhou, T. Zhang, J. Arbiol, X. H. Lu*, B.-W. Mao, X. Zhang*, J. Fransaer*

Hierarchical porous Ni_3S_4 with enriched high-valence Ni sites as a robust electrocatalyst for efficient oxygen evolution reaction

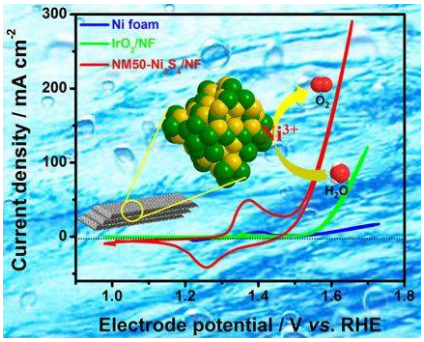

Supporting Information

Hierarchical porous Ni_3S_4 with enriched high-valence Ni sites as a robust electrocatalyst for efficient oxygen evolution reaction

Kai Wan, Jiangshui Luo*, Chen Zhou, Ting Zhang, Jordi Arbiol, Xihong Lu*, Bing-Wei Mao, Xuan Zhang*, Jan Fransaer*

1. Electrode preparation

The catalyst dispersion was prepared as follows: 5.0 mg of the catalyst was dispersed in 400 μL EtOH + 40 μL 5 wt. % Nafion (Nafion® DE 520, Sigma-Aldrich) + 60 μL deionized water by sonification for 30 min.

For the GC electrode, 10 μL of the catalyst dispersion was dropped onto the glassy carbon electrode (GCE) by using a pipette and then dried at room temperature. The catalyst loading of the electrode was 500 μg cm^{-2}.

For the Ni foam electrode, 300 μL of the catalyst dispersion was dropped on a Ni foam (1 cm × 1 cm) to reach a catalyst loading of 3.0 mg cm^{-2}. The Ni foam was sonificated successively in ethanol, acetone and diluted hydrochloric acid (4.0 M) for 10 min, respectively, to remove the possible grease and oxide on the surface. Then it was washed with deionized water to be neutral and subsequently dried under vacuum at 60 °C.

The IrO_2 and 10 wt. % Pt/C catalysts dispersions were also dropped onto the GCE or Ni foam with the same method of Ni_3S_4. The catalyst loading for GC electrode: 500 μg cm^{-2} (IrO_2); for Ni foam electrodes: 3.0 mg cm^{-2} (IrO_2, 10 wt. % Pt/C 3.0 mg cm^{-2}).

2. Calibration of reference electrode potentials

All potentials are calibrated to the RHE potential based on Nernst equation:

$$E_{\mathrm{RHE}} = E^{\ominus}_{\mathrm{Hg/HgO}} + 0.0591 \times \mathrm{pH} \quad (1)$$

where $E^{\ominus}_{\mathrm{Hg/HgO}}$ is the standard electrode potential of the Hg/HgO electrode (0.098 V *vs.* SHE), and T is room temperature (298.15 K).

3. *iR*-corrections

All potentials are *iR*-corrected to compensate for the influence of solution resistances, using the following equation:

$$E_{\mathrm{iR-corrected}} = E - iR \quad (2)$$

where i is the current and R is the uncompensated ohmic electrolyte resistance measured by

EIS.

4. Overpotential (η)

The overpotential (η) is calculated using the following equation:

$$\eta = E_{\mathrm{iR-corrected}} - 1.23 \quad (3)$$

5. Tafel slope

The Tafel slope is determined by fitting polarization data to the Tafel equation:

$$\eta = \mathrm{a} + \mathrm{b} * \log|j| \quad (4)$$

where η is the overpotential, b is the Tafel slope, and j is the current density.

6. The Krasil'shcikov path:

Tafel slopes are usually used to describe the primary activities of OER. Generally, the commonly accepted mechanism for the OER in alkaline media is the Krasil'shcikov path, as shown in equations (5)−(8).[1-3]

$$* + OH^- \rightarrow *\text{-}OH + e^- \quad \text{Tafel slope: 120 mV dec}^{-1} \quad (5)$$

$$*\text{-}OH + OH^- \rightarrow *\text{-}O^- + H_2O \quad \text{Tafel slope: 60 mV dec}^{-1} \quad (6)$$

$$*\text{-}O^- \rightarrow *\text{-}O + e^- \quad \text{Tafel slope: 40 mV dec}^{-1} \quad (7)$$

$$2*\text{-}O \rightarrow 2* + O_2 \uparrow \quad \text{Tafel slope: 15 mV dec}^{-1} \quad (8)$$

where * is an active site of the catalyst.

7. Faradaic efficiency

The Faradic efficiency of the catalyst for the OER is defined as the ratio of the experimentally measured volume of oxygen evolved divided by the theoretical volume of O_2 based on the ideal gas law the Faraday law. The measurements of the volume of O_2 were performed in a home-made electrolytic cell by water drainage method. A constant current of 0.1 A on an electrode with an area of 1 cm^2 (1 cm × 1 cm) was applied for 300 s, 600 s, 900 s, and 1200 s, respectively, to produce O_2 during the measurements.

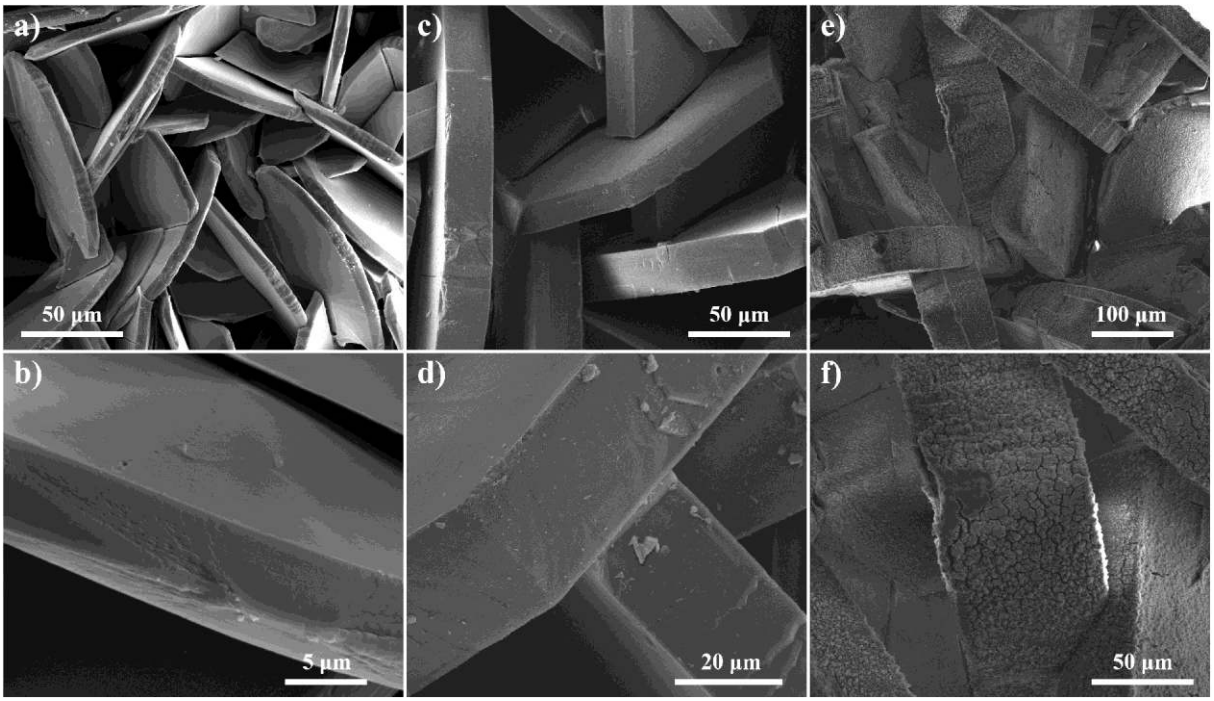

Figure S1. SEM images of the Ni-MOFs: a-b) NM50, c-d) NM80, e-f) NM120.

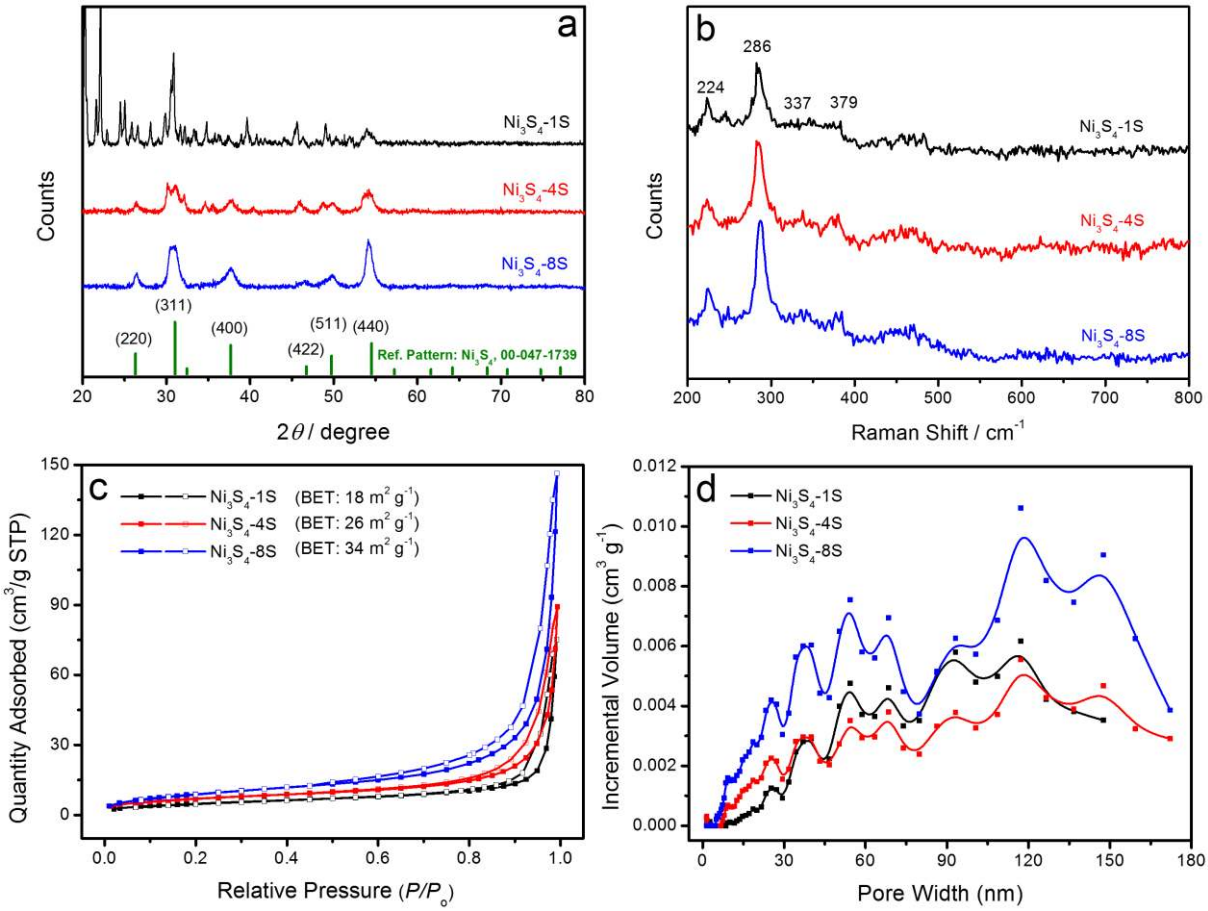

Figure S2. a) X-ray diffraction (XRD) patterns of the Ni_3S_4 samples. b) Raman spectra of the Ni_3S_4 samples. c) Nitrogen ad/desorption isotherms of the Ni_3S_4 samples. d) The corresponding pore size distribution.

In the synthesis process of Ni_3S_4, the sulfurization conditions were first investigated by using NM50 as the self-sacrificial templates. The molar ratios of the sulfur ion to Ni-MOF were fixed at 1 : 1, 4 :1 , and 8 : 1, and the obtained Ni_3S_4 were denoted as Ni_3S_4-1S, Ni_3S_4-4S, Ni_3S_4-8S, respectively. It can be seen from Figure S2a that the sample synthesized with a molar ratio of 1 : 1 (sulfur ion *vs*. Ni salt) exhibits a different XRD pattern, which may be due to the incomplete sulfurization when using a low molar ratio of S *vs.* Ni. When the molar ratio of sulfur to Ni increased gradually, a typical diffraction pattern of cubic phase of Ni_3S_4 (JCPDS: 00-047-1739) can be observed.

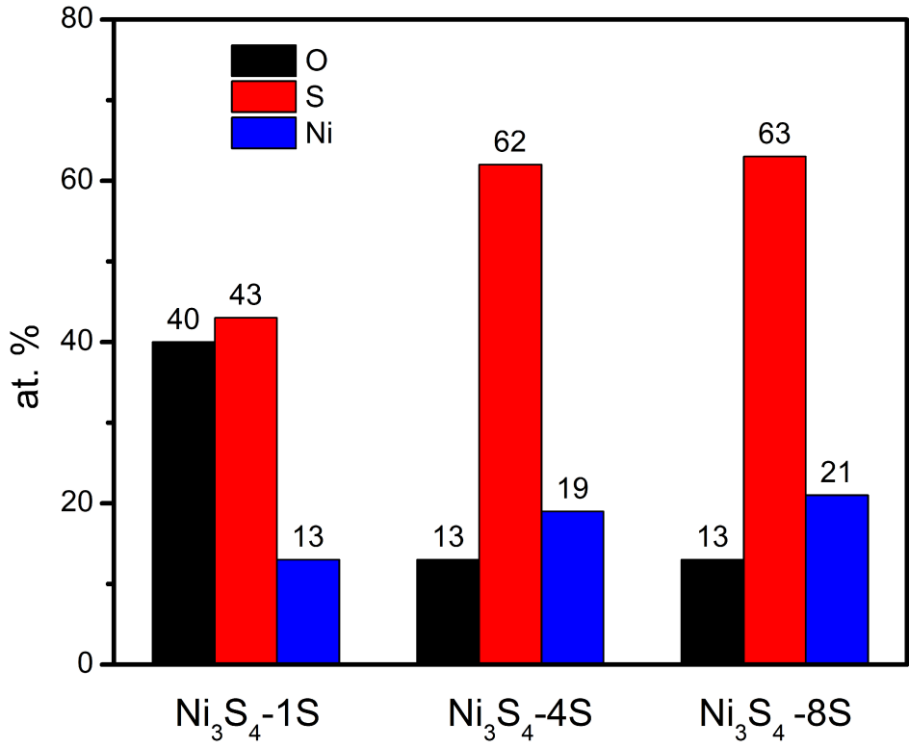

Figure S3. Elemental composition (at. %) of the Ni_3S_4 obtained from EDS plane scan.

The Ni_3S_4 materials synthesized with a molar ratio (sulfur ion *vs*. Ni salt) of 4 : 1 and 8 : 1 exhibit almost the same content of O, Ni, and S. Therefore, a molar ratio of sulfur to Ni-MOF of 8 : 1 was selected for the synthesis of Ni_3S_4, and the resulting Ni_3S_4 samples are denoted as NM50-Ni_3S_4, NM80-Ni_3S_4, and NM120-Ni_3S_4, respectively.

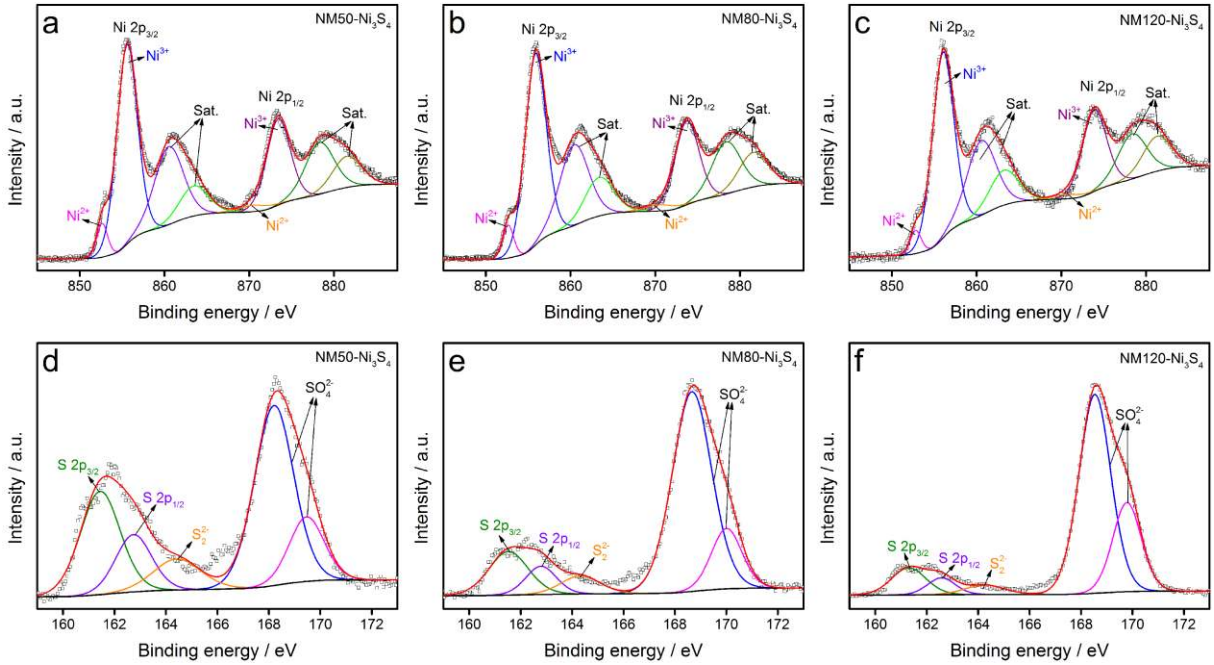

Figure S4. Ni 2p peaks and the peak fitting results: a) NM50-Ni_3S_4, b) NM80-Ni_3S_4, c) NM120-Ni_3S_4. S 2p peak and the peak fitting results: d) NM50-Ni_3S_4, e) NM80-Ni_3S_4, f) NM120-Ni_3S_4.

The Ni 2p spectrum was deconvoluted into eight peaks, which are assigned to the Ni $2p_{3/2}$, Ni $2p_{1/2}$, and the satellite peaks. For the Ni $2p_{3/2}$, the binding energies at 852.99, 852.93, 852.64, 852.64 and 852.80 eV and 856.57, 586.50, 855.59, 855.88 and 856.03 eV were assigned to Ni^{2+} and Ni^{3+}, respectively.[4, 5] And the peaks at 860.35 ± 0.2 eV and 863.35 ± 0.2 eV were assigned to the satellite peaks (referred as 'Sat.' in the figure), which indicate the presence of nickel–oxygen species.[6-8]

The S 2p spectrum was deconvoluted into five peaks. The three peaks at around 161.3 eV, 162.6 eV, and 164.3 eV were attributed to the S $2p_{3/2}$ of S^{2-}, S $2p_{1/2}$ of S^{2-}, and the bridging S_2^{2-} (referred to as 'SO_4^{2-}'), respectively.[9-11] The peaks at 168.4 eV and 169.7 eV were assigned to the sulfates resulting from the surface oxidation of the Ni_3S_4.[11, 12]

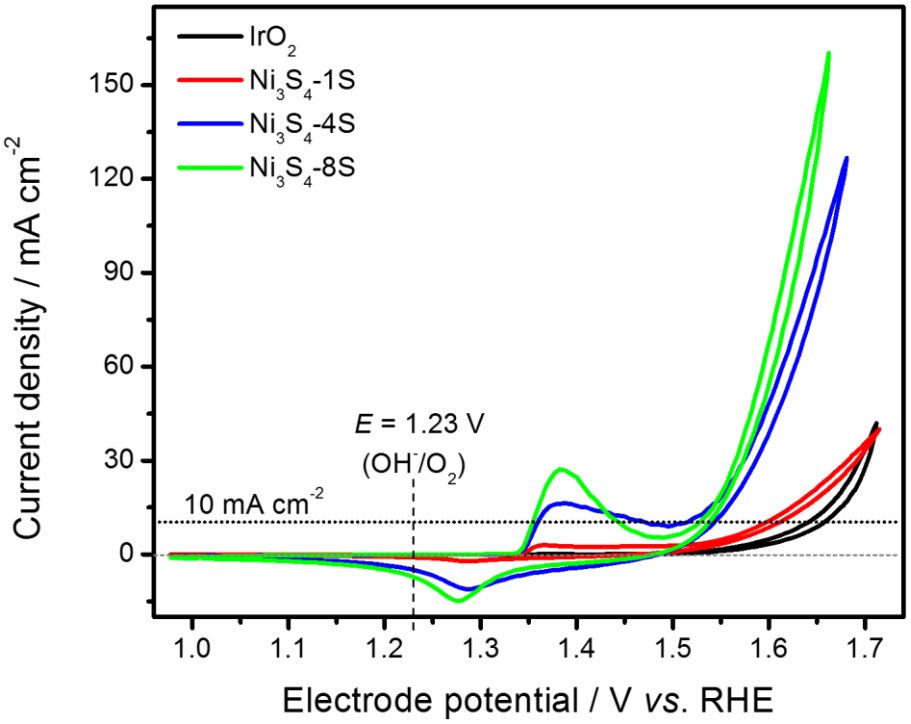

Figure S5. Cyclic voltammograms of the Ni_3S_4 samples in 1.0 M KOH at a scan rate of 10 mV s^{-1} at 1600 rpm, showing the OER polarization curves (the molar ratios of the sulfur ion to Ni-MOF were fixed at 1:1, 4:1 and 8:1, and the obtained Ni_3S_4 were denoted as Ni_3S_4-1S, Ni_3S_4-4S, Ni_3S_4-8S, respectively.).

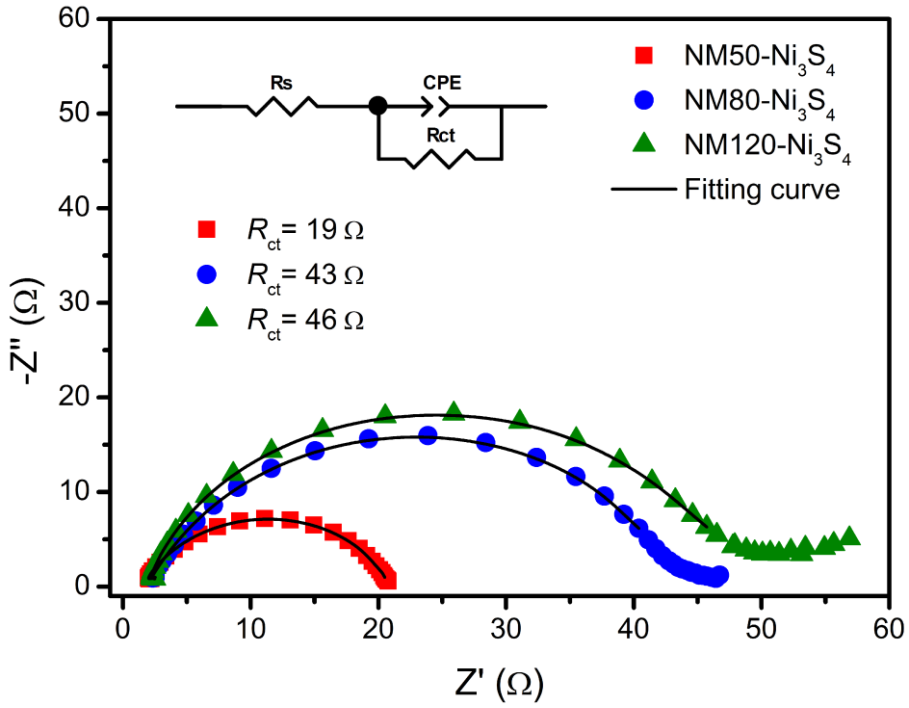

Figure S6. Nyquist plots and fitting results of the Ni_3S_4 catalysts in the frequency range from 100 kHz to 0.1 Hz with an amplitude of 5 mV (peak-to-peak) at 1.61 V *vs.* RHE. Inset is the equivalent circuit, where R_s is the resistance of the electrolyte, R_{ct} is the charge transfer resistance, and CPE the constant phase element.

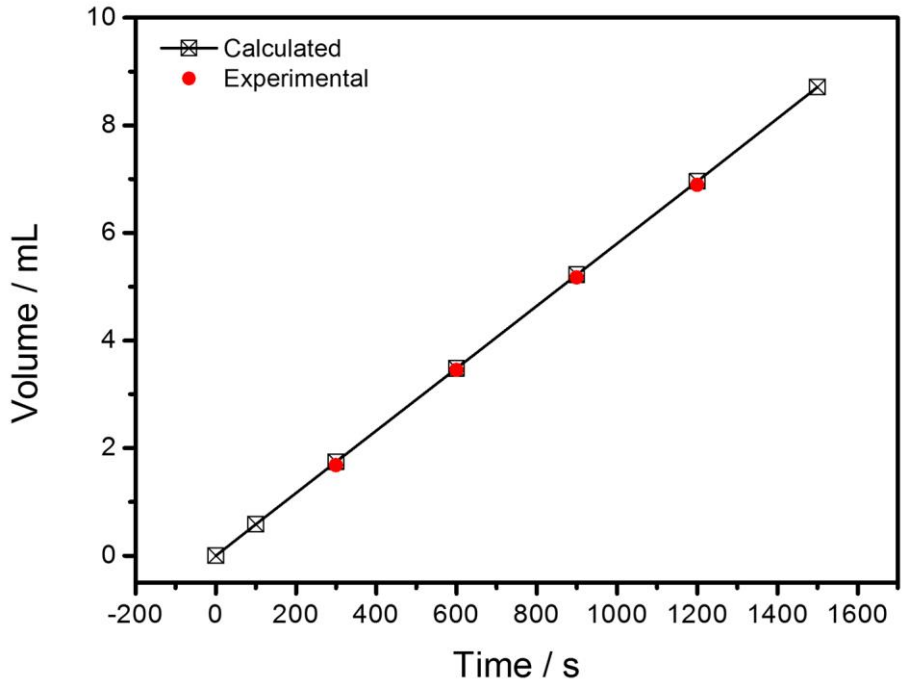

Figure S7. The theoretical and experimental amounts of O_2 evolved during the OER in 1.0 M KOH solution at 100 mA cm^{-2} as a function of time.

The Faradaic efficiency of NM50-Ni_3S_4 for the OER was found to be around 99%, indicating that nearly all of the current was used for the evolution of oxygen.

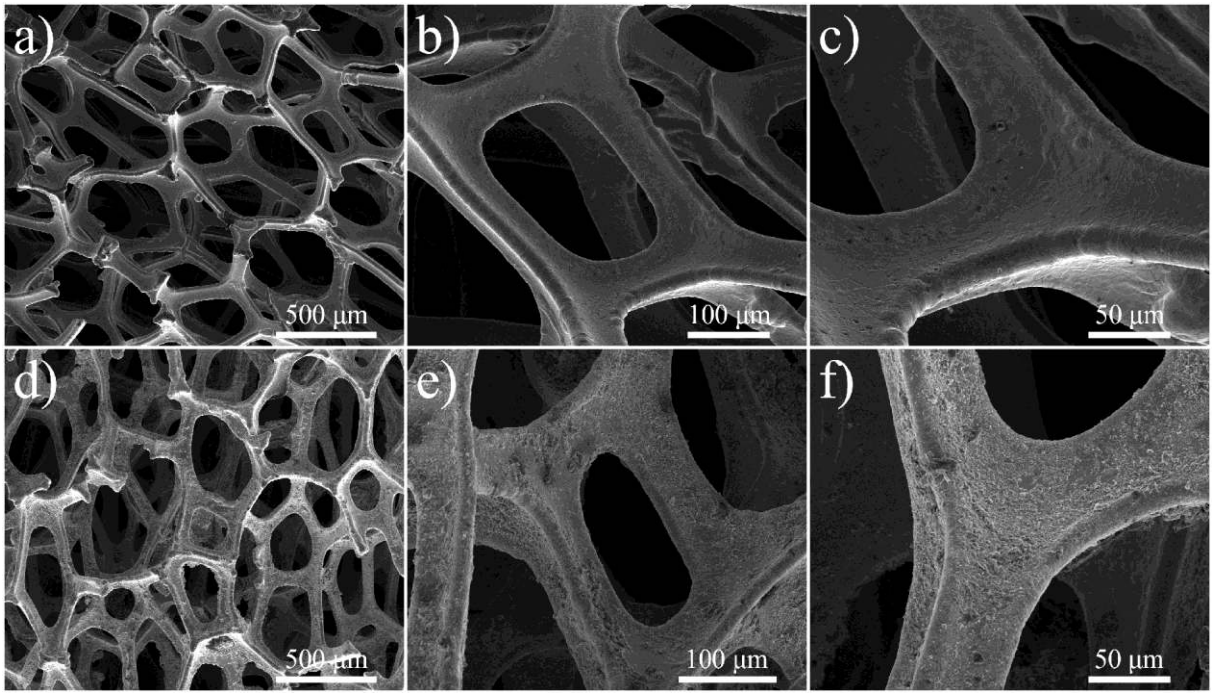

Figure S8. SEM images: a-c) Ni foam, d-f) the NM50-Ni_3S_4/NF electrode.

Clearly, the catalyst was coated on the surface of the Ni foam successfully.

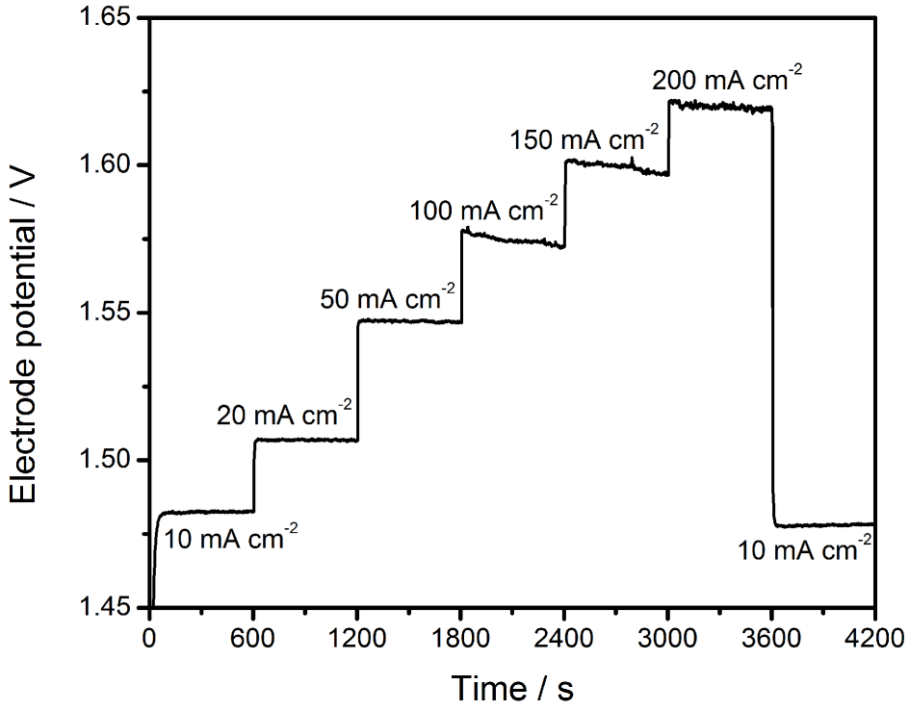

Figure S9. Staircase chronopotentiometric curves of NM50-Ni_3S_4/NF electrode for OER recorded at different current densities in 1.0 M KOH.

The staircase chronopotentiometric curves of a NM50-Ni_3S_4/NF electrode for OER at current densities from 10 to 200 mA cm^{-2} were recorded. The potentials at 10 mA cm^{-2} exhibit a small decrease even after the chronopotentiometric test at 200 mA cm^{-2}, which may be due to the oxidation of the Ni foam thus increasing the OER activity.

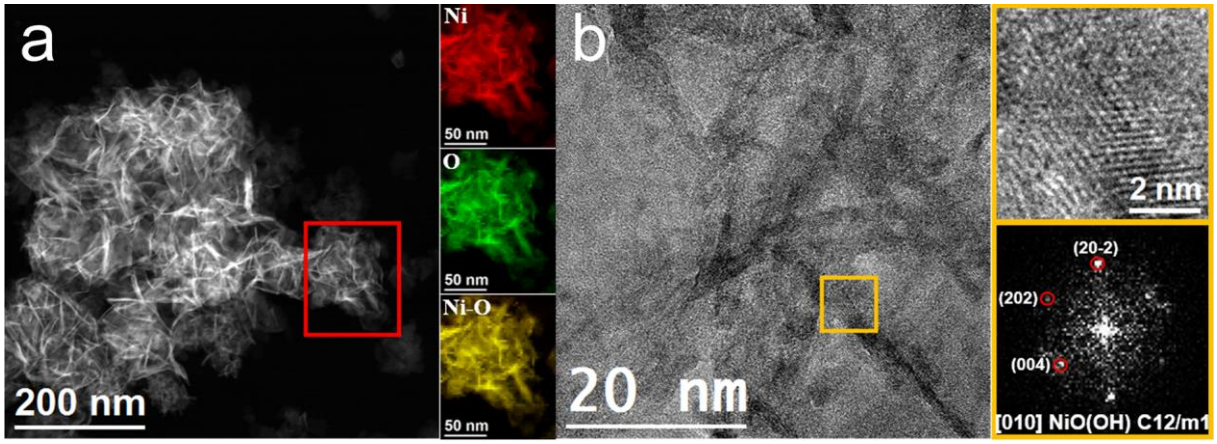

Figure S10. a) EELS chemical composition maps of NM50-Ni_3S_4 after OER (100 h test at 50 mA cm^{-2}) obtained from the area highlighted in red of the STEM micrograph; b) HR-TEM micrograph of NM50-Ni_3S_4 after OER, details of the area highlighted in orange and its corresponding power spectrum.

It can be seen that the sample derived from theNi_3S_4 catalyst after the long duration test shows sheet-like nanostructures. The EELS mapping images indicate the existence of Ni and O after OER test. This result confirms the loss of S under oxidative environments of the OER, which is consistent with the previous reports.[13-16] The HR-TEM result reveals that the selected nanocrystal structure is in agreement with the NiO(OH) monoclinic phase (space group: C12/m1) with $a = b = c = 8.1140$ Å. The NiO(OH) lattice fringe distances were measured to be 0.217 nm, 0.209 nm and 0.245 nm at 56.00º and 66.36º which could be interpreted as the monoclinic NiO(OH) phase, visualized along its [010] zone axis. The high content of high-valence Ni^{3+} in the Ni_3S_4 catalyst facilitates the formation of active NiOOH, which benefits the chemisorption of OH^- during OER.

Table S1. Bulk plane spacing distances and the angles between planes: experimental *vs*. theoretical.

Spot	Experimental (nm)	Ni_3S_4 (Fd3mS) $[01\bar{1}]$
1	0.536	0.546 (111)
2	0.493(54.9º *vs.* Spot 1)	0.473 (54.74º) (200)
3	0.551 (112.35º *vs.* Spot 1)	0.546 (109.47º) $(1\bar{1}\bar{1})$
4	0.242 (54.09º *vs.* Spot 1)	0.236 (54.74º) (400)

From the crystalline domain, the Ni_3S_4 lattice fringe distances were measured to be 0.536 nm, 0.493 nm, 0.551 and 0.242 nm, the latter three of which were at angles of 54.91º, 112.35º and 54.09º, which could be interpreted as the cubic Ni_3S_4 phase, visualized along its $[01\bar{1}]$ zone axis.

Table S2. Elemental composition (at. %) of the resultant nickel sulfides measured by XPS.

Sample	C	N	O	S	Ni
NM50-Ni_3S_4	21.1	0.9	50.5	18.3	9.2
NM80-Ni_3S_4	19.3	0.9	54.2	17.3	8.3
NM120-Ni_3S_4	34.2	0.5	45.2	14.1	6.0

Table S3. The content of each Ni component (%) of the obtained Ni_3S_4 catalysts based on Figure S4, indicating the greater exposure of Ni^{3+} sites over Ni^{2+} sites at the surface of Ni_3S_4.

Sample	Ni^{2+}			Ni^{3+}			Ni−O species
	$2p_{1/2}$	$2p_{3/2}$	Total	$2p_{1/2}$	$2p_{3/2}$	Total	Total
NM50-Ni_3S_4	1.49	2.99	4.48	16.80	33.61	50.41	45.11
NM80-Ni_3S_4	1.42	2.84	4.26	16.10	32.19	48.29	47.45
NM120-Ni_3S_4	1.06	2.12	3.18	16.85	33.71	50.56	46.26

Table S4. The content of each S component (%) of the Ni_3S_4 catalysts based on Figure S4.

Sample	S^{2-}			S_2^{2-}	S−O species
	$2p_{1/2}$	$2p_{3/2}$	Total	Total	Total
NM50-Ni_3S_4	12.15	24.29	36.44	8.74	54.82
NM80-Ni_3S_4	6.63	13.26	19.89	5.46	74.65
NM120-Ni_3S_4	4.40	8.79	13.19	3.52	83.29

Table S5. Comparison of the OER catalytic performance of the NM50-Ni_3S_4/NF electrode and the metal sulfides reported in literature (on Ni foam in 1.0 M KOH).

Catalyst	Catalyst loading / mg cm^{-2}	Overpotential / mV	Stability	References
Ni_3S_4-8-NiMOF@50	**3.0**	**257 @ 10 mA cm^{-2} 270 @ 20 mA cm^{-2} 300 @ 50 mA cm^{-2} 340 @ 100 mA cm^{-2}**	**at 50 mA cm^{-2} for 300 h**	**This work**
RA-Ni_3S_2	-	260 @ 10 mA cm^{-2} 340 @ 100 mA cm^{-2}	at η = 300 mV for 50 h	[17]
Elox_H_2S_NF	-	258 @ 10 mA cm^{-2}	-	[14]
NiS	43	335 @ 50 mA cm^{-2}	at η = 290 mV for 20 h	[18]
$Ni(OH)_2/Ni_3S_2$	-	270 @ 20 mA cm^{-2}	at η = 270 mV for 10 h	[19]
Co_3O_4@Ni_3S_2	-	260 @ 20 mA cm^{-2}	at 10 mA cm^{-2} for 12 h	[20]
CdS/Ni_3S_2	1.75	280 @ 10 mA cm^{-2}	at η = 270 mV for 12 h	[21]
S-$NiFe_2O4$	-	267 @ 10 mA cm^{-2}	at η = 420 mV for 24 h	[22]
Ni-Mo-S	-	390 @ 10 mA cm^{-2}	at 15 mA cm^{-2} for 12 h	[23]
Co_9S_8@NOSC-900	5.0	330 @ 20 mA cm^{-2} 420 @ 100 mA cm^{-2}	at 10 mA cm^{-2} for 10 h	[24]
$Mo_{(1-x)}W_xS_2$	-	285 @ 10 mA cm^{-2}	at 10 mA cm^{-2} for 50 h	[25]
MoS	25	310 @ 20 mA cm^{-2} (1.0 M NaOH)	-	[26]
CoS-$Co(OH)_2$@aMoS_{2+x}	0.2	380 @ 10 mA cm^{-2}	at 10 mA cm^{-2} for 28 h	[27]

References

[1] E. L. Miller, R. E. Rocheleau, *J. Electrochem. Soc.* **1997**, 144, 3072.

[2] H. Xiao, H. Shin, W. A. Goddard, *Proc. Natl. Acad. Sci. U. S. A.* **2018**, 115, 5872.

[3] S. Gupta, L. Qiao, S. Zhao, H. Xu, Y. Lin, S. V. Devaguptapu, X. Wang, M. T. Swihart, G. Wu, *Adv. Energy Mater.* **2016**, 6, 1601198.

[4] X. Ma, L. Zhang, G. Xu, C. Zhang, H. Song, Y. He, C. Zhang, D. Jia, *Chem. Eng. J.* **2017**, 320, 22.

[5] B. Guan, Y. Li, B. Yin, K. Liu, D. Wang, H. Zhang, C. Cheng, *Chem. Eng. J.* **2017**, 308, 1165.

[6] K. Lian, S. Thorpe, D. Kirk, *Electrochim. Acta* **1992**, 37, 2029.

[7] P. Selvam, B. Viswanathan, V. Srinivasan, *J. Electron Spectrosc. Relat. Phenom.* **1989**, 49, 203.

[8] B. Konkena, J. Masa, A. J. R. Botz, I. Sinev, W. Xia, J. Koßmann, R. Drautz, M. Muhler, W. Schuhmann, *ACS Catal.* **2017**, 7, 229.

[9] F. Huang, Y. W. Sui, F. X. Wei, J. Q. Qi, Q. K. Meng, Y. Z. He, *J. Mater. Sci.: Mater. Electron.* **2018**, 29, 2525.

[10] Z. Zhang, Q. Wang, C. Zhao, S. Min, X. Qian, *ACS Appl. Mater. Interfaces* **2015**, 7, 4861.

[11] J. Lv, Y. Cheng, W. Liu, B. Quan, X. Liang, G. Ji, Y. Du, *J. Mater. Chem. C* **2018**, 6, 1822.

[12] T. Tian, L. Huang, L. Ai, J. Jiang, *J. Mater. Chem. A* **2017**, 5, 20985.

[13] S. Jin, *ACS Energy Lett.* **2017**, 2, 1937.

[14] M. Lee, H.-S. Oh, M. K. Cho, J.-P. Ahn, Y. J. Hwang, B. K. Min, *Appl. Catal. B Environ.* **2018**, 233, 130.

[15] K. Fan, H. Zou, Y. Lu, H. Chen, F. Li, J. Liu, L. Sun, L. Tong, M. F. Toney, M. Sui, J. Yu, *ACS Nano* **2018**, 12, 12369.

[16] B. R. Wygant, K. Kawashima, C. B. Mullins, *ACS Energy Lett.* **2018**, 3, 2956.

[17] L. Zeng, K. Sun, Z. Yang, S. Xie, Y. Chen, Z. Liu, Y. Liu, J. Zhao, Y. Liu, C. Liu, *J. Mater. Chem. A* **2018**, 6, 4485.

[18] W. Zhu, X. Yue, W. Zhang, S. Yu, Y. Zhang, J. Wang, J. Wang, *Chem. Commun.* **2016**, 52, 1486.

[19] X. Du, Z. Yang, Y. Li, Y. Gong, M. Zhao, *J. Mater. Chem. A* **2018**, 6, 6938.

[20] Y. Gong, Z. Xu, H. Pan, Y. Lin, Z. Yang, X. Du, *J. Mater. Chem. A* **2018**, 6, 5098.

[21] S. Qu, J. Huang, J. Yu, G. Chen, W. Hu, M. Yin, R. Zhang, S. Chu, C. Li, *ACS Appl. Mater. Interfaces* **2017**, 9, 29660.

[22] J. Liu, D. Zhu, T. Ling, A. Vasileff, S.-Z. Qiao, *Nano Energy* **2017**, 40, 264.

[23] Z. Ma, H. Meng, M. Wang, B. Tang, J. Li, X. Wang, *ChemElectroChem* **2018**, 5, 335.

[24] S. Huang, Y. Meng, S. He, A. Goswami, Q. Wu, J. Li, S. Tong, T. Asefa, M. Wu, *Adv. Funct. Mater.* **2017**, 27, 1606585.

[25] M. Zheng, J. Du, B. Hou, C. L. Xu, *ACS Appl. Mater. Interfaces* **2017**, 9, 26066.

[26] K. Yan, Y. Lu, *Small* **2016**, 12, 2975.

[27] T. Yoon, K. S. Kim, *Adv. Funct. Mater.* **2016**, 26, 7386.